Article Information

Article Title: Magnetic Field Effect on Threshold Voltage for Ultrathin Silicon Gate-All-Around Nanowire Field-Effect-Transistors

Journal Name: Silicon

Author Names: Hamdy Abdelhamid - Azza M. Anis - Mohamed E. Aboulwafa - Mohamed I. Eladawy

Affiliation:

Hamdy Abdelhamid (corresponding author)

at Center of Nano-Electronics and Devices (CND), Zewail City of Science and Technology, 6th October City 12588, Egypt

Email: hamdy.abdelhamid@gmail.com

Azza M. Anis - Mohamed E. Aboulwafa - Mohamed I. Eladawy

at Electronics, Communications, and Computers Department, Faculty of Engineering, Helwan University, Helwan 11795, Egypt

Noname manuscript No.
(will be inserted by the editor)

Magnetic Field Effect on Threshold Voltage for Ultrathin Silicon Gate-All-Around Nanowire Field-Effect-Transistors

Hamdy Abdelhamid · Azza M. Anis · Mohamed E. Aboulwafa · Mohamed I. Eladawy

the date of receipt and acceptance should be inserted later

Abstract Gate-all-around silicon nanowire field-effect-transistors (GAA Si NWFETs) received much interest in nanoscale electronic based systems and sensor applications. In this work, the threshold voltage for the ultrathin lightly doped n-channel Si GAA NWFETs with magnetic field effect is investigated. The study begins by modeling the inversion charge density including confinement-effect in the channel cross-section of the device. Three-dimensional (3D) potential model including magnetic field interaction is studied in this work. Threshold voltage and short channel effects such as threshold voltage roll-off and drain induced barrier lowering are also analyzed at different channel lengths. The obtained analytical results have been verified with 3D COMSOL numerical simulation results. The impact of the external magnetic field is well observed in the energy dispersion relations. However, the magnetic field has no considerable effect on the threshold voltage neither the short channel behavior for the proposed Si GAA NWFET even with increasing the biasing values and at different device parameters.

Keywords Ultrathin Si GAA NWFETs · Threshold voltage · Short channel effects · Zeeman effect · Quantum confinement

Hamdy Abdelhamid (corresponding author)
Center of Nano-Electronics and Devices (CND), Zewail City of Science and Technology, 6th October City 12588, Egypt
E-mail: hamdy.abdelhamid@gmail.com

Azza M. Anis · Mohamed E. Aboulwafa · Mohamed I. Eladawy
Electronics, Communications, and Computers Department, Faculty of Engineering, Helwan University, Helwan 11795, Egypt

1 Introduction

As complementary-metal-oxide-semiconductor (CMOS) technology reached to the nano-meter scale, numbers of challenges are facing the conventional CMOS Transistors. Among of these problems are the short channel effects that degrade the device-performance such as threshold voltage roll-off, drain induced barrier lowering, and subthreshold-swing. Others related to the quantum mechanical effects that increase overall leakage current such as carrier-confinement and tunneling. To overcome the device-performance degradation problems that facing CMOS industry, alternative design architectures such as fin field-effect-transistors (FinFETs) [1,2], tunnel FETs [3], and nanowire (NW) FETs [4] have been recommended.

Gate-all-around (GAA) based NWFETs are believed to be one of the dominant structures that extend the scaling limit of the conventional single-gate MOSFET down to nanoscale-range for the future technology-nodes [5–8]. GAA NWFET is advantageous over the classical-devices due to its significant reduction of the short channel limitations, lower parasitic-capacitances, lower off-current, improved current-capability, and transconductance [9–11].

Several models have been presented to depict operation and characteristics of different cross-sectional channel shapes of GAA NWFETs. In [12,13], deep comparison between square and circular cross-sectional areas has been given by simulations based on different numerical methods. For each configuration, threshold voltage, subthreshold-swing, current ratio I_{on}/I_{off}, and transconductance have been evaluated. GAA NWFET drain current, charges, and capacitances models have been presented in [14]. Random dopant fluctuation effects have been considered in the undoped n-channel

GAA NWFETs by Nayak et al. and Sung et al. [15, 16]. Subthreshold characteristics comprising quantum confinement effects on the device have been analytically modeled [17]. Moreover, GAA NWFET potential model and current analysis for different transport techniques have been released by Michetti et al., Sharma and Vishvakarma [18, 19]. Threshold voltage models for diminutive channel quadruple-gate MOSFETs including electrons confinement-effects have been reported in [20–22]. Khan et al. figured out the charge and the gate capacitance through introducing numerical models for surrounding gate MOSFET in [23]. The subthreshold current and subthreshold-swing are studied in [24–26] for the quadruple-gate MOSFETs whereas the quantum confinement is taken into account in [27].

Studying the impact of the surrounding magnetic field on characteristics of GAA NWFETs becomes an essential demand when the device used in electronic circuits [28, 29] and sensor applications [30, 31]. The magnetic field may be applied directly or induced from the electric-field through the Lorentz transformation [32]. Most of the available GAA NWFET models disregard the magnetic field effects in their works. Hence, it is essential to develop advanced models that describe these physical effects on the device-performance definitely for scaling the device down to nano-meter scale. Our objective in this paper is to study the influence of applied magnetic field on subthreshold characteristics of the lightly doped ultrathin silicon GAA NWFET, Fig. 1.

This work is arranged as follows: Density of mobile carriers and charge density including both two-dimensional (2D) confinement-effect and Zeeman interaction are reported in Section 2. A 3D potential model of the ultrathin lightly doped Si GAA NWFETs is also developed in this section. The threshold voltage and the short channel effects (SCEs) are modeled in Section 2. The models are verified with the 3D numerical simulation results in Section 3. The conclusions, and main achievements of this work, are introduced in Section 4.

2 Device Characteristics

2.1 Inversion Charge Density

In the existence of magnetic field on the channel region, an interaction, which arises from the Zeeman's effect, should be considered. The Zeeman interaction can be defined as:

$$H_z = \frac{g^* \mu_B}{2} \sigma.B \tag{1}$$

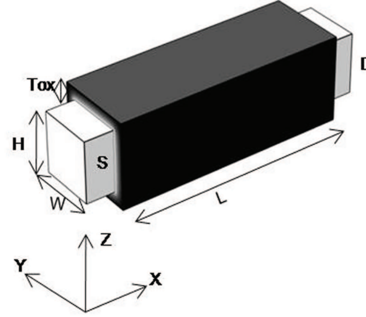

Fig. 1 Structure representation of the GAA NWFET used in this work, S (D) stands for source (drain) region, L, H, W, for length, height, width of channel region, respectively, and T_{ox} for oxide thickness

where g^* is the effective electron g-factor, μ_B is the Boher-magneton, σ is the vector of the Pauli-matrices, and B is the magnetic field strength.

The electron energy along the transport direction incorporating Zeeman interaction is given by:

$$E_x = \frac{\hbar^2 k_x^2}{2m_x} \pm \delta_B B \tag{2}$$

here m_x is the effective mass along the transport direction of electron, $\hbar$ is the reduced Plank-constant, and $\delta_B = \frac{g^* \mu_B}{2}$. The second term in Eq. (2) represents the Zeeman shift in energy due to the external applied magnetic field B.

The wave vector (k_x) can be formed as:

$$k_x = \sqrt{\frac{2m_x E_x}{\hbar^2}} \left(1 \pm \frac{\delta_B B}{E_x}\right)^{0.5} \tag{3}$$

Let $\mu = \pm\frac{\delta_B B}{E_x}$ and for $|\mu| < 1$, Eq. (3) can be expanded by the binominal-theorem [33]:

$$(1+\mu)^n = \sum_{i=0}^{\infty} \binom{n}{i} \mu^i \tag{4}$$

$$\binom{n}{i} = \frac{n(n-1)...(n-i+1)}{i!} \tag{5}$$

into,

$$k_x = \sqrt{\frac{2m_x E_x}{\hbar^2}} \sum_{i=0}^{\infty} \binom{0.5}{i} \left(\frac{\pm\delta_B B}{E_x}\right)^i \tag{6}$$

The Schrodinger equation describing the squared cross-section of the structure shown in Fig. 1 can be expressed as:

$$\frac{\hbar^2}{2m_y}\frac{\partial^2\psi}{\partial y^2}+\frac{\hbar^2}{2m_z}\frac{\partial^2\psi}{\partial z^2}+(E_n-E_c)\,\psi=0 \tag{7}$$

where ψ is the wave function of the electron and m_y, m_z are the effective masses along the confinement directions.

The quantized energy (E_n) measured from the conduction band edge (E_c) has been obtained as [34]:

$$E_n-E_c=\frac{(\pi\hbar)^2}{2}\left(\frac{n_y^2}{m_yW^2}+\frac{n_z^2}{m_zH^2}\right) \tag{8}$$

The electron total energy (E) for the square cross-sectional area of the GAA NWFET can then be written as:

$$E(k_x,n_y,n_z)=\frac{\hbar^2k_x^2}{2m_x}+\frac{(\pi\hbar)^2}{2}\left(\frac{n_y^2}{m_yW^2}+\frac{n_z^2}{m_zH^2}\right)+E_c\pm\delta_BB \tag{9}$$

The density of states (DOS) for all subbands (n) and valleys (v) can be computed by:

$$DOS=\sum_{n,v}g_v\sqrt{\frac{m_d^v}{2\pi^2\hbar^2}}\frac{1}{\sqrt{(E-E_n^v)\pm\delta_BB}} \tag{10}$$

where g_v is the degeneracy of valley and m_d^v is the effective mass at different valleys $m_d^{1,2}=m_t$ (transverse-mass) and $m_d^3=m_l$ (longitudinal-mass)

From Eq. (8) and Eq. (10), the one-dimensional electron concentration (n_e) can be calculated from:

$$n_e=\int_{E_n^v}^{\infty}DOS.f(E)dE \tag{11}$$

Employing the Fermi-Dirac-distribution, $f(E)=\left(1+e^{\frac{E-E_F}{KT}}\right)^{-1}$ into Eq. (11) gives:

$$n_e=\sum_{n,v}g_v\sqrt{\frac{m_d^vKT}{2\pi\hbar^2}}[f_{\frac{-1}{2}}(\eta)+\left(\frac{\delta_BB}{KT}\right)f_{\frac{-3}{2}}(\eta)+\frac{1}{2}\left(\frac{\delta_BB}{KT}\right)^2f_{\frac{-5}{2}}(\eta)+\frac{1}{6}\left(\frac{\delta_BB}{KT}\right)^3f_{\frac{-7}{2}}(\eta)+\dots] \tag{12}$$

where $\eta=(E_F-E_n^v)/KT$, E_F is Fermi-energy, K is Boltzmann-constant, and T is temperature.

Fermi-Dirac-integral of order λ can be computed from $f_\lambda(\eta)\approx\int_0^\infty\frac{\xi^\lambda d\xi}{1+e^{\xi-\eta}}$, [35].

Charge density $(Q_e=qn_e)$ can be calculated from the Boltzmann-approximation, i.e., $f(E)\approx e^{-\left(\frac{E-E_F}{KT}\right)}$ as:

$$Q_e=qQ_0(B)\sum_{n,v}g_v\sqrt{\frac{m_d^vKT}{2\pi\hbar^2}}e^{\frac{(E_F-E_c)}{KT}}e^{\frac{-E^v(n_y,n_z)}{KT}} \tag{13}$$

$$E^v(n_y,n_z)=\frac{(\pi\hbar)^2}{2}\left(\frac{n_y^2}{m_y^vW^2}+\frac{n_z^2}{m_z^vH^2}\right) \tag{14}$$

$$\begin{aligned}(m_y^1,m_z^1)&=(m_t,m_l)\\(m_y^2,m_z^2)&=(m_l,m_t)\\(m_y^3,m_z^3)&=(m_t,m_t)\end{aligned} \tag{15}$$

$Q_0(B)$ is the reliance of carrier density on magnetic field and can be evaluated from:

$$Q_0(B)=1+\left(\frac{\delta_BB}{KT}\right)+\frac{1}{2}\left(\frac{\delta_BB}{KT}\right)^2+\frac{1}{6}\left(\frac{\delta_BB}{KT}\right)^3 \tag{16}$$

The other higher order terms can be ignored due to their little contribution.

2.2 Electrostatic Potential

The electrostatic potential for Si GAA NWFET including the mobile-charges can be calculated from the solution of the 3D Poisson equation, or

$$\frac{\partial^2V(x,y,z)}{\partial x^2}+\frac{\partial^2V(x,y,z)}{\partial y^2}+\frac{\partial^2V(x,y,z)}{\partial z^2}=\frac{qn_e}{WH\epsilon_{si}}e^{\frac{qV(x,y,z)}{KT}} \tag{17}$$

The boundary conditions of Eq. (17), can be written as:

$$\frac{\pm\epsilon_{ox}}{\epsilon_{si}T_{ox}}\left(V_{gs}-\phi_{ms}-V(x,y,z)|_{y=\mp\frac{W}{2}}\right)=\frac{\partial V(x,y,z)}{\partial y}|_{y=\pm\frac{W}{2}} \tag{18}$$

$$\frac{\pm\epsilon_{ox}}{\epsilon_{si}T_{ox}}\left(V_{gs}-\phi_{ms}-V(x,y,z)|_{z=\mp\frac{H}{2}}\right)=\frac{\partial V(x,y,z)}{\partial z}|_{z=\pm\frac{H}{2}} \tag{19}$$

$$V(x,y,z)|_{x=0}=V_{bi} \tag{20}$$

$$V(x,y,z)|_{x=L}=V_{bi}+V_{ds} \tag{21}$$

here V_{gs} is the gate to source voltage, V_{ds} is the drain to source voltage, V_{bi} is the built-in voltage between source/drain and the channel, ϕ_{ms} is the metal to the surface work function, T_{ox} is thickness of oxide, ϵ_{si} and ϵ_{ox} are Si and oxide permitivities, respectively.

By applying the superposition-principle [36] on Eq. (17) and utilizing boundary conditions from Eqs. (18) to (21), one obtains (see the Appendix)

$$V(x,y,z) = V_0(y) + RV_1(x,y,z) + V_2(x,y,z) + V_3(y)z^2 \tag{22}$$

$$V_1(x,y,z) = -\cos(\alpha_y y)\cos(\alpha_z z)\cos(\alpha_y/2)\frac{C_0(x)}{K_1} \tag{23}$$

$$V_2(x,y,z) = \cos(\alpha_y y)\cos(\alpha_z z)[V_{ds}C_1(x) + V_{bi}C_0(x)]\frac{K_0}{K_1} \tag{24}$$

$$V_3(y) = \frac{V_{gs} - \phi_{ms} - V_0(y)}{1 - \frac{4\epsilon_{si}T_{ox}}{\epsilon_{ox}H}} \tag{25}$$

$$C_0(x) = \frac{\sinh(\alpha_x x) - \sinh(\alpha_x(x-L))}{\sinh(\alpha_x L)} \tag{26}$$

$$C_1(x) = \frac{\sinh(\alpha_x x)}{\sinh(\alpha_x L)} \tag{27}$$

The potential along the channel thickness ($V_0(y)$) can be given by:

$$\frac{\partial^2 V_0(y)}{\partial y^2} = \frac{qn_e}{WH\epsilon_{si}}e^{\frac{qV_0(y)}{KT}} \tag{28}$$

with,

$$\frac{\pm\epsilon_{ox}}{\epsilon_{si}T_{ox}}\left(V_{gs} - \phi_{ms} - V_0(y)|_{y=\frac{\mp W}{2}}\right) = \frac{\partial V_0(y)}{\partial y}|_{y=\frac{\mp W}{2}} \tag{29}$$

$$\frac{\partial V_0(y)}{\partial y}|_{y=0} = 0 \tag{30}$$

After some mathematical-manipulations [37], we found that:

$$V_0(y) = V_t \ln\left(\beta_n^2 \frac{8V_t\epsilon_{si}}{qn_e W^2}\sec^2(\beta_n y)\right) \tag{31}$$

The virtual-cathode point is located at x_{min} and can be found from:

$$\frac{\partial V(x,y,z)}{\partial x}|_{x=x_{min}} = 0 \tag{32}$$

by,

$$x_{min} = \frac{L}{2} - \frac{1}{2\alpha_x}\ln\left(\frac{A}{D}\right) \tag{33}$$

$$A = \frac{K_0\left(V_{ds} + V_{bi}(1-e^{-\alpha_x L})\right)}{K_1(1-e^{-2\alpha_x L})} - \frac{R\cos(\alpha_y/2)(1-e^{-\alpha_x L})}{K_1(1-e^{-2\alpha_x L})} \tag{34}$$

$$D = \frac{K_0}{K_1}\left(V_{bi} - \frac{V_{ds} + V_{bi}(1-e^{-\alpha_x L})}{2\sinh(\alpha_x L)}\right) - \frac{R\cos(\alpha_y/2)}{K_1}\left(1 - \frac{1-e^{-\alpha_x L}}{2\sinh(\alpha_x L)}\right) \tag{35}$$

The coefficients of Eq. (34) and Eq. (35) are defined in the Appendix.

2.3 Threshold Voltage

Threshold voltage classically is defined by the gate voltage at which the minimum surface potential reaches to twice the bulk potential [38,39]. Another definition for threshold voltage has been introduced in [36,40], which assuming the threshold-condition can be computed when the carrier charge density reaches to a point called "virtual-cathode", Q_c that is sufficient to turn the device on, and we will consider this definition for our work.

Please notice that, quantum threshold voltage is determined using square-potential-well-approximation [20,27]. The minimal of the approximated well equals to conduction band edge, or

$$E_c = \frac{E_g}{2} - qV(x_{min}, y_c, z_c) \tag{36}$$

here y_c and z_c are the position of the conduction-path of the device [36]. By utilizing Eq. (22) into Eq. (36) the quantum threshold voltage can be written as:

$$V_{th} = \frac{\frac{E_g}{2q} + V_t\ln\left(\frac{Q_c}{\rho}\right) + V_tV_1(x_{min},y_c,z_c)}{1 + 4K_2V_1(x_{min},y_c,z_c)} - \frac{V_2(x_{min},y_c,z_c)}{1 + 4K_2V_1(x_{min},y_c,z_c)} \tag{37}$$

ρ can be computed from:

$$\rho = qQ_0(B)[\sqrt{\frac{2m_tKT}{\pi\hbar^2}}(e^{\frac{-E^1(1,1)}{KT}} + e^{\frac{-E^2(1,1)}{KT}}) + \sqrt{\frac{2m_lKT}{\pi\hbar^2}}e^{\frac{-E^3(1,1)}{KT}}] \tag{38}$$

When the magnetic field is neglected (i.e., $B = 0$), Eq. (16) simplifies to $Q_0(B) = 1$ and the ρ factor will be reduced to the analytical expression given by Kumar and Mahapatra [20].

By subtracting the long-channel threshold voltage that is given by $V_{th,long} = \frac{E_g}{2q} + V_t\ln\left(\frac{Q_c}{\rho}\right)$, the threshold voltage roll-off (Roll-Off) is found as,

$$Roll\!-\!Off = \frac{-4K_2V_1(x_{min},y_c,z_c)\left(\frac{E_g}{2q} + V_t\ln\left(\frac{Q_c}{\rho}\right)\right)}{1 + 4K_2V_1(x_{min},y_c,z_c)} + \frac{V_tV_1(x_{min},y_c,z_c) - V_2(x_{min},y_c,z_c)}{1 + 4K_2V_1(x_{min},y_c,z_c)} \tag{39}$$

Drain induced barrier lowering (DIBL) of ultrathin GAA NWFET can be determined from the difference between the threshold voltage ($V_{th,high}$) at high drain to source voltage ($V_{ds,high}$) and the threshold voltage ($V_{th,low}$) at low drain to source voltage ($V_{ds,low}$) or,

$$DIBL = -\frac{V_{th,high} - V_{th,low}}{V_{ds,high} - V_{ds,low}} \tag{40}$$

The carrier charge density at virtual-cathode (Q_c), can be expressed as [20–22, 27, 36]:

$$Q_c = qn_iWHe^{\frac{qV(x_{min},y_c,z_c)}{KT}} \quad (41)$$

here, 3D numerical simulations of the considered GAA NWFET indicate that $Q_c \approx 1.5.10^9 WH\ m^{-1}$, $y_c = 0.80.y$, and $z_c = 0.95.z$.

3 Results and Discussion

In this work, the device parameters used are: lightly doped n-channel with doping concentration $N_a = 10^{12} : 10^{15}\ cm^{-3}$, length $L = 20\ nm$, height $H = 5\ nm$, width $W = 5\ nm$, and gate oxide thickness $T_{ox} = 1\ nm$.

The numerical results for the GAA NWFET are obtained from the 3D-finite-elements based simulation using COMSOL Multiphysics [41]. The 3D Poisson equation introduced in Eq. (17) has been simulated using the "general-form partial-differential-equation" application mode. The quantum correction and the Zeeman's interaction were successfully employed. The physical-parameters and the boundary conditions were checked and successfully are achieved.

The energy band along transport direction is indicated versus wave vector in Fig. 2 before and after applying magnetic field. In the existence of magnetic field ($B = 1\ Tesla$), the central energy band is vertically split into two subbands and the energy separation, ΔE (where $\Delta E = g^*\mu_B B$). The splitting between two branches is controlled by the applied magnetic field value.

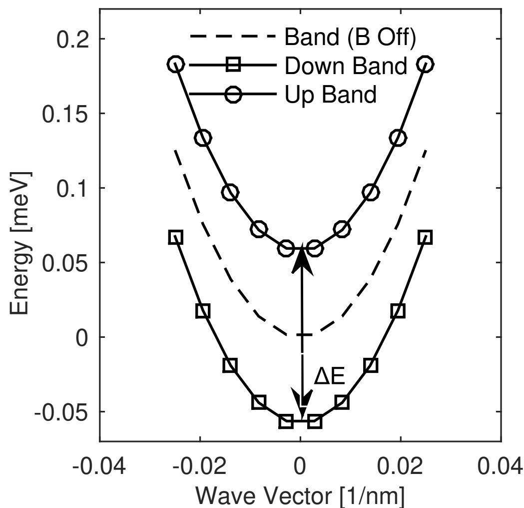

Fig. 2 Energy spectrum versus wave vector including the effect of applied magnetic field at $B = 1\ Tesla$

Figure 3 indicates the results of the potential model derived in Eq. (22) along the channel length with and without magnetic field. Results were calculated for different values of: drain to source voltage (Fig. 3a), cross-section parameters (Fig. 3b), oxide thickness (Fig. 3c), and channel-doping concentration (Fig. 3d). As shown in Fig. 3, an excellent matching between the analytical model and the numerical simulation results. The exterior magnetic field has negligible effect on the channel potential even at different values of applied voltage and device parameters. Thus, the electrostatic potential of Si GAA NWFET has immunity to applied magnetic field due to the small value of electron g-factor for silicon ($g^* = 2$, [42, 43]).

On the contrary, the III-V semiconductors such as indium antimonide which is used as a magnetic field sensor because of its large value of electron g-factor ($|g^*| = 51$, [44–46]).

Figure 4 shows the channel potential contours including the effect of the external magnetic field with different metal work functions ($\phi_m = 4.5\ eV$ in Fig. 4a while $\phi_m = 4.8\ eV$ in Fig. 4b). From Fig. 4, we can confirm that the potential model is valid at several values of metal work function. The effect of the magnetic field on the channel potential of Si GAA NWFETs has insignificant effect even at different values for the metal work function. In [47], the authors achieved experimentally that the magnetic field has insignificant effect on thick and long-channel single-gate bulk-MOSFETs. In [48], the authors studied the spin-orbit coupling only on the NWFET using a complex numerical technique called k.p model.

Figure 5 shows threshold voltage variations against length of channel at different values of drain to source voltage with and without external magnetic field. As shown, the threshold voltage model, introduced in Eq. (37), is highly consistent with the numerical simulations obtained from COMSOL. The threshold voltage values of Si GAA NWFETs are almost identical before and after applying magnetic field in agreement with the results outlined in [47].

Figures 6, 7 display threshold voltage roll-off (Roll-Off) and drain induced barrier lowering (DIBL) as a function of channel length with and without magnetic field. As seen, the Roll-Off and the DIBL models agree very well with COMSOL results. The magnetic field has negligible effect on the short channel effect parameters such as Roll-Off and DIBL of Si GAA NWFETs.

The obtained results indicate that threshold characteristics for Si GAA NWFET are insensitive to external magnetic field even at large applied values.

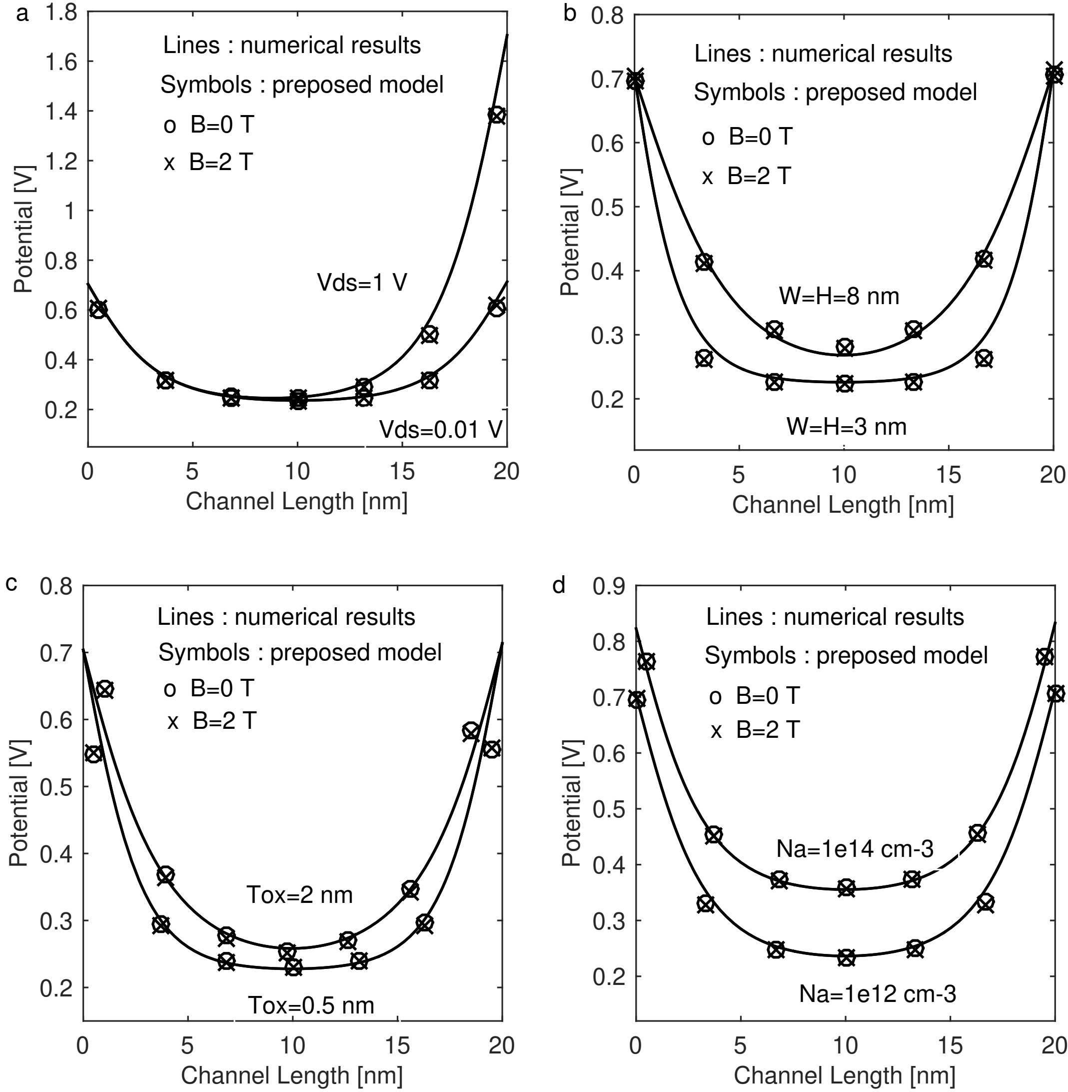

Fig. 3 Potential variation with channel length for Si GAA NWFET when the existence ($B = 2\ Tesla$ cross markers) and disappearing ($B = 0\ Tesla$ circular markers) of external magnetic field at dfferent values of: a drain to source voltage (V_{ds}), b cross section parameters (W and H), c oxide thickness (T_{ox}), and d channel doping concentration (N_a), respectivily

4 Conclusion

Threshold voltage of lightly doped Si GAA NWFETs incorporating magnetic field effect on the channel has been developed. Models for device characteristics such as energy sub-bands, density of states including the quantum confinement and magnetic field effects were included. The 3D electrostatic potential, Roll-Off, and DIBL have been also computed. Analytical results show reasonable matching with that from COMSOL numerical simulations. From the given analysis, we conclude that the intensity of the magnetic field has insignificant effect on threshold voltage for Si GAA NWFET.

5 Appendix

The solution of 3D Poisson equation Eq. (17), can be calculated by:

$$V(x, y, z) = V_l(y, z) + V_s(x, y, z) \tag{42}$$

$V_l(y, z)$ is the long-channel potential-solution in y-z plane obtained by solving,

$$\frac{\partial^2 V_l(y, z)}{\partial y^2} + \frac{\partial^2 V_l(y, z)}{\partial z^2} = \frac{q n_e}{W H \epsilon_{si}} e^{\frac{q V_l(y,z)}{KT}} \tag{43}$$

The potential $V_l(y, z)$ can be represented as:

$$V_l(y, z) = V_0(y) + V_1(y)z + V_3(y)z^2 \tag{44}$$

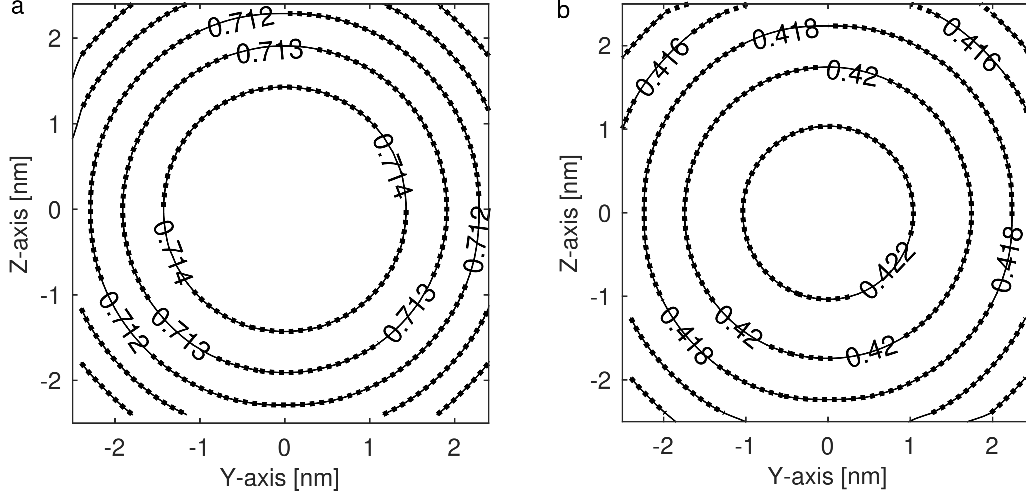

Fig. 4 Electrostatic potential contours for Si GAA NWFET of y-z plane at $x = L/2$, a represents $\phi_m = 4.5\ eV$ and b represents $\phi_m = 4.8\ eV$, lines for $B = 0\ Tesla$ and symbols for $B = 2\ Tesla$

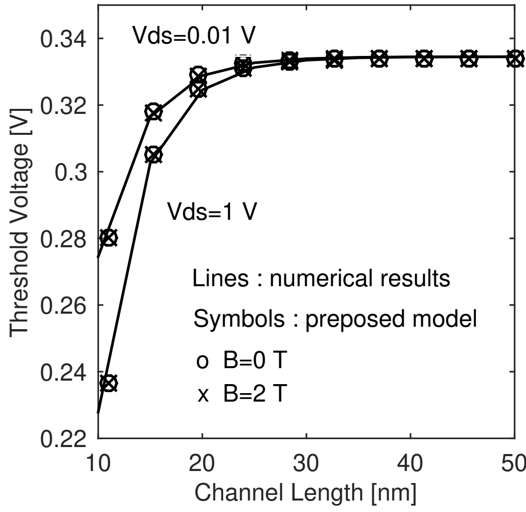

Fig. 5 Threshold voltage variation with channel length when the existence ($B = 2$ Tesla cross markers) and the absence ($B = 0$ Tesla circular markers) of magnetic field at different values of drain to source voltage (V_{ds})

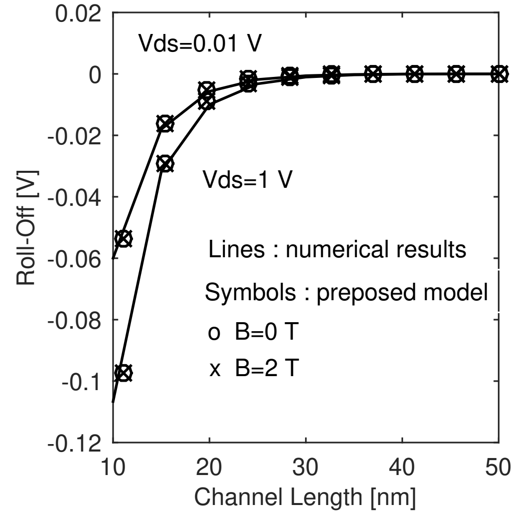

Fig. 6 Roll-Off versus channel length including magnetic field effect at different values of drain to source voltage (V_{ds})

Expressions for $V_1(y)$ and $V_3(y)$ can be calculated from:

$$\frac{\pm\epsilon_{ox}}{\epsilon_{si}T_{ox}}\left(V_{gs} - \phi_{ms} - V_l(y,z)|_{z=\frac{\mp H}{2}}\right) = \frac{\partial V_l(y,z)}{\partial z}|_{z=\frac{\mp H}{2}} \quad (45)$$

yield, $V_1(y) = 0$ and $V_3(y)$ can be represented by Eq. (25).

$V_s(x, y, z)$ is the solution of the short-channel potential that obtained by solving,

$$\frac{\partial^2 V_s(x,y,z)}{\partial x^2} + \frac{\partial^2 V_s(x,y,z)}{\partial y^2} + \frac{\partial^2 V_s(x,y,z)}{\partial z^2} = 0 \quad (46)$$

The potential $V_s(x, y, z)$ can be written as:

$$V_s(x,y,z) = [S_1 e^{\alpha_x(x-L)} + S_2 e^{-\alpha_x x}][S_3\cos(\alpha_z z) + S_4\sin(\alpha_z z)]\cos(\alpha_y y) \quad (47)$$

The constants S_1, S_2, S_3, and S_4 can be obtained from the boundary conditions Eq. (20) and Eq. (21).

Definitions for the coefficients in the text can be calculated by:

$$R = 4K_2V_0(y = 0.5) + 8K_2K_3V_3(y = 0.5) - V_t \quad (48)$$

$$K_0 = \frac{4\sin(\alpha_y)\sin(\alpha_z)}{\alpha_y\alpha_z} \quad (49)$$

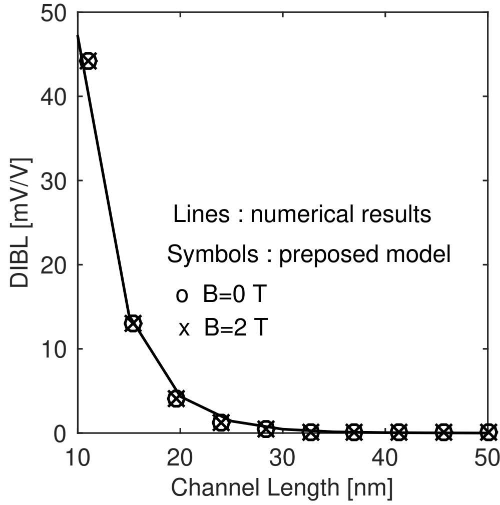

Fig. 7 DIBL against channel length including magnetic field effect

$$K_1 = \frac{2\alpha_z + \sin(2\alpha_z)}{2\alpha_z} \tag{50}$$

$$K_2 = \frac{\sin(\alpha_z)}{\alpha_z} \tag{51}$$

$$K_3 = \frac{1}{2} - \frac{1}{\alpha_z^2} + \frac{\cos(\alpha_z)}{\alpha_z \sin(\alpha_z)} \tag{52}$$

Eigen values α_x, α_y, and α_z can be computed from:

$$\frac{\epsilon_{ox} W}{2\epsilon_{si} T_{ox}} + \alpha_y \tan(\alpha_y) = 0 \tag{53}$$

$$\frac{\epsilon_{ox} H}{2\epsilon_{si} T_{ox}} + \alpha_z \tan(\alpha_z) = 0 \tag{54}$$

$$\alpha_x = \sqrt{\left(\frac{2\alpha_y}{W}\right)^2 + \left(\frac{2\alpha_z}{H}\right)^2} \tag{55}$$

β_n has been defined when solving the equation,

$$\frac{V_{gs} - \phi_{ms}}{2V_t} - \ln\left(\frac{2}{W}\sqrt{\frac{2V_t \epsilon_{si}}{q n_e}}\frac{\beta_n}{\cos(\beta_n)}\right) - \frac{2\epsilon_{si} T_{ox}}{\epsilon_{ox} W}\beta_n \tan(\beta_n) = 0 \tag{56}$$

$$V_t = \frac{KT}{q} \tag{57}$$

$$V_{bi} = V_t \ln\left(\frac{N_a N_d}{n_i^2}\right) \tag{58}$$

$$\phi_{ms} = \phi_m - \left(\chi + \frac{E_g}{2} + V_t \ln\left(\frac{N_a}{n_i}\right)\right) \tag{59}$$

here n_i is intrinsic concentration, N_a is the acceptor concentration in channel, N_d is the donor concentration in the source and the drain regions, ϕ_m is the metal work function, q is charge of electron, χ is electron affinity, and E_g is the energy gap.

References

1. Saremi M, Kusha AA, Mohammadi S (2012) Ground plane fin-shaped field effect transistor (GP-FinFET): a FinFET for low leakage power circuits. Microelectronic Engineering 95:74-82
2. Elthakeb AT, Elhamid HA, Ismail Y (2015) Scaling of TG-FinFETs: 3-D monte carlo simulations in the ballistic and quasi-ballistic regimes. IEEE Trans Electron Devices 62:1796-1802
3. Imenabadi RM, Saremi M, Vandenberghe WG (2017) A novel pnpn-like z-shaped tunnel field-effect transistor with improved ambipolar behavior and RF performance. IEEE Trans Electron Devices 64:4752-4758
4. Abadi RMI, Saremi M (2018) A resonant tunneling nanowire field effect transistor with physical contractions: a negative differential resistance device for low power very large scale integration applications. Journal of Electronic Materials 47:1091-1098
5. Elhamid HA, Iniguez B, Guitart JR (2007) Analytical model of the threshold voltage and subthreshold swing of undoped cylindrical gate-all-around-based MOSFETs. IEEE Trans Electron Devices 54:572-579
6. Yeh MS, Lee YJ, Hung MF, Liu KC, Wu YC (2013) High-performance gate-all-around poly-Si thin-film transistors by microwave annealing with NH3 plasma passivation. IEEE Trans Nanotechnol 12:636-640
7. Kumar S, Kumari A, Das MK (2016) Modeling gate-all-around Si/SiGe MOSFETs and circuits for digital applications. Journal of Computational Electronics 16:47-60
8. Nagy D, Indalecio G, Loureiro AJG, Elmessary MA, Kalna K, Seoane N (2018) FinFET versus gate-all-around nanowire FET: performance, scaling, and variability. IEEE Journal of the Electron Devices Society 6:332-340
9. Panda SR, Sharma R, Pradhan KP, Sahu PK (2016) Junctionless GAA nanowire transistor: towards circuit application. Int Conf ICEE :1-4
10. Prakash O, Beniwal S, Maheshwaram S, Bulusu A, Singh N, Manhas SK (2017) Compact NBTI reliability modeling in Si nanowire MOSFETs and effect in circuits. IEEE Trans Device Mater Reliab 17:404-413
11. Yao J, Li J, Luo K, Yu J, Zhang Q, Hou Z, Gu J, Yang W, Wu Z, Yin H, Wang W (2018) Physical insights on quantum confinement and carrier mobility in Si, $Si_{0.45}Ge_{0.55}$, Ge gate-all-around NSFET for 5 nm technology node. IEEE Journal of the Electron Devices Society 6:841-848
12. Bayani AH, Dideban D, Voves J, Moezi N (2017) Investigation of sub-10nm cylindrical surrounding gate germanium nanowire field effect transistor with different cross-section areas. Superlattices and Microstructures 105:110-116
13. Bayani AH, Voves J, Dideban D (2018) Effective mass approximation versus full atomistic model to calculate the output characteristics of a gate-all-around germanium nanowire field effect transistor (GAA-GeNW-FET). Superlattices and Microstructures 113:769-776
14. Gaidhane AD, Pahwa G, Verma A, Chauhan YS (2018) Compact modeling of drain current, charges, and capacitances in long-channel gate-all-around negative capacitance MFIS transistor. IEEE Trans Electron Devices 65:2024-2032
15. Nayak K, Agarwal S, Bajaj M, Mural KVRM, Rao VR (2015) Random dopant fluctuation induced variability in undoped channel Si gate all around nanowire n-MOSFET. IEEE Trans Electron Devices 62:685-688
16. Sung WL, Chao PJ, Li Y (2017) Timing and power fluctuations on gate-all-around nanowire CMOS circuit induced

by various sources of random discrete dopants. Int Conf SISPAD
17. Elkashlan RY, Elhamid HA, Ismail YI (2018) Two-dimensional models for quantum effects on short channel electrostatics of lightly doped symmetric double-gate MOSFETs. IET Circuits, Devices & Systems 12:341-346
18. Michetti P, Mugnaini G, Iannaccone G (2009) Analytical model of nanowire FETs in a partially ballistic or dissipative transport regime. IEEE Trans Electron Devices 56:1402-1410
19. Sharma D, Vishvakarma SK (2012) Analytical modeling for 3D potential distribution of rectangular gate (RecG) gate-all-around (GAA) MOSFET in subthreshold and strong inversion regions. Microelectronics Journal 43:358-363
20. Kumar PR, Mahapatra S (2011) Quantum threshold voltage modeling of short channel quad gate silicon nanowire transistor. IEEE Trans Nanotech 10:121-128
21. Pricilla A, Pandian MK, Balamurugan NB (2013) Potential and quantum threshold voltage modeling of gate-all-around nanowire MOSFETs. Active and Passive Electronic Components
22. Pandian MK, Balamurugan NB (2014) Analytical threshold voltage modeling of surrounding gate silicon nanowire transistors with different geometries. J Electr Eng Technol 9:2079-2088
23. Khan SUZ, Hossain MS, Hossen MO, Rahman FU, Zaman R, Khosru QDM (2014) Self-consistent capacitance-voltage characterization of gate-all-around graded nanowire transistor. arXiv:1406.5257v1 [cond-mat.mtrl-sci]
24. Jit S, Samoju VR, Tiwari PK (2014) A quasi-3D threshold voltage model for dual-metal quadruple-gate MOSFETs. Chin Phys Lett 31:128502-1-128502-3
25. Dubey S, Samoju VR, Tiwari PK (2015) Quasi-3D subthreshold current and subthreshold swing models of dual-metal quadruple-gate (DMQG) MOSFETs. Journal of Computational Electronics 14:582-592
26. Samoju VR, Tiwari PK (2016) Threshold voltage modeling for dual-metal quadruple-gate (DMQG) MOSFETs. Int J Numer Model 29:695-706
27. Mahapatra K, Samoju VR, Tiwari PK (2017) Analytical modeling of subthreshold characteristics by considering quantum confinement effects in ultrathin dual-metal quadruple gate (DMQG) MOSFETs. Superlattices and Microstructures 111:704-713
28. Mongillo M, Spathis P, Katsaros G, Gentile P, Franceschi SD (2012) Multifunctional devices and logic gates with undoped silicon nanowires. Nano Lett 12:3074-3079
29. Marchi MD, Zhang J, Frache S, Sacchetto D, Gaillardon PE, Leblebici Y, Micheli GD (2014) Configurable logic gates using polarity-controlled silicon nanowire gate-all-around FETs. IEEE Electron Device Lett 35:880-882
30. Zhang S, Lou L, Gu Y (2017) Development of silicon nanowire–based NEMS absolute pressure sensor through surface micromachining. IEEE Electron Device Lett 38:653-656
31. Pratap Y, Kumar M, Kabra S, Haldar S, Gupta RS, Gupta M (2017) Analytical modeling of gate-all-around junctionless transistor based biosensor for detection of neutral biomolecule species. Journal of Computational Electronics 17:1-9
32. Ivezic T (2016) Nature of electric and magnetic fields; how the fields transform. arXiv:1508.04802v2 [physics.gen-ph]
33. Gupta P (2011) Comprehensive mathematics xi. Laxmi Publications (P) LTD
34. Harrison P, Valavanis A (2016) Quantum wells, wires and dots: theoretical and computational physics of semiconductor nanostructures. John Wiley & Sons, LTD
35. Kim R, Lundstrom M (2011) Notes on Fermi-Dirac integrals. arXiv:0811.0116v4 [cond-mat.mes-hall]
36. Elhamid HA, Iniguez B, Kilchytska V, Flandre D, Ismail Y (2015) An analytical 3D model for short-channel effects in undoped FinFETs. Journal of Computational Electronics 14:500-505
37. Gradshteyn IS, Ryzhik IM (2014) Tables of integrals, series and products. Academic Press
38. Chiang TK (2009) A new compact subthreshold behavior model for dual-material surrounding gate (DMSG) MOSFETs. Solid-State Electronics 53:490-496
39. Pradhan KP, Kumar MR, Mohapatra SK, Sahu PK (2015) Analytical modeling of threshold voltage for cylindrical gate all around (CGAA) MOSFET using center potential. Ain Shams Engineering Journal 6:1171-1177
40. Tiwari PK, Dubey S, Singh M, Jit S (2010) A two-dimensional analytical model for threshold voltage of short-channel triple-material double-gate metal-oxide-semiconductor field-effect transistors. J Appl Phys 108:074508-1-074508-8
41. COMSOL Multiphysics. http://www.comsol.com.
42. Konakov AA, Ezhevskii AA, Soukhorukov AV, Guseinov DV, Popkov SA, Burdov VA (2011) Lande factor of the conduction electrons in silicon: temperature dependence. J Phys Conf Ser. https://doi.org/10.1088/1742-6596/324/1/012027
43. Giorgioni A, Paleari S, Cecchi S, Vitiello E, Grilli E, Isella G, Jantsch W, Fanciulli M, Pezzoli F (2016) Strong confinement-induced engineering of the g-factor and lifetime of conduction electron spins in Ge quantum wells. Nat Commun. https://doi.org/10.1038/ncomms13886
44. Kosaka H, Kiselev AA, Baron FA, Kim KW, Yablonovitch E (2001) Electron g factor engineering in III-V semiconductors for quantum communications. Electronics Letters 37:464-465
45. Litvinenko KL, Nikzad L, Pidgeon CR, Allam J, Cohen LF, Ashley T, Emeny M, Zawadzki W, Murdin BN (2008) Temperature dependence of the electron Lande g factor in InSb and GaAs. Phys Rev B 77:033204-1-033204-4
46. Qu F, Veen J, Vries FK, Beukman AJA, Wimmer M, Yi W, Kiselev AA, Nguyen BM, Sokolich M, Manfra MJ, Nichele F, Marcus CM, Kouwenhoven LP (2016) Quantized conductance and large g-factor anisotropy in InSb quantum point contacts. Nano Lett 16:7509-7513
47. Hofflin J, Sander C, Gieschke P, Greiner A, Korvink JG (2015) Subthreshold CMOS transistors are largely immune to magnetic field effects when operated above 11 T. Concepts Magn Reson Part B: Magn Reson Eng 45:97-105
48. Shin M, Lee S, Klimeck G (2010) Computational study on the performance of Si nanowire PMOSFETs based on the k.p method. IEEE Trans Electron Devices 57:2274-2283